



Topology optimization of reactive material structures for penetrative projectiles

Shinyu Kim ^a, Saekyeol Kim ^a, Taekyun Kim ^a, Sangin Choi ^a, Tae Hee Lee ^{a,*},
Jung Su Park ^b, Sang-Hyun Jung ^b

^a Department of Automotive Engineering, Hanyang University, 222 Wangsimni-ro, Seongdong-gu, Seoul, 04763, Republic of Korea

^b The 4th R&D Institute, Agency for Defense Development, 35, Yuseong P.O. Box, Daejeon, 34186, Republic of Korea

ARTICLE INFO

Article history:

Received 29 May 2020

Received in revised form

6 March 2021

Accepted 6 May 2021

Available online xxx

Keywords:

Reactive material

Penetrative projectile

Topology optimization

Manufacturing constraint

Cold gas dynamic spray

Additive manufacturing

ABSTRACT

Recently, reactive materials have been developed for penetrative projectiles to improve impact resistance and energy capacity. However, the design of a reactive material structure, involving shape and size, is challenging because of difficulties such as high non-linearity of impact resistance, manufacturing limitations of reactive materials and high expenses of penetration experiments. In this study, a design optimization methodology for the reactive material structure is developed based on the finite element analysis. A finite element model for penetration analysis is introduced to save the expenses of the experiments. Impact resistance is assessed through the analysis, and result is calibrated by comparing with experimental results. Based on the model, topology optimization is introduced to determine shape of the structure. The design variables and constraints of the optimization are proposed considering the manufacturing limitations, and the optimal shape that can be manufactured by cold spraying is determined. Based on the optimal shape, size optimization is introduced to determine the geometric dimensions of the structure. As a result, optimal design of the reactive material structure and steel case of the penetrative projectile, which maximizes the impact resistance, is determined. Using the design process proposed in this study, reactive material structures can be designed considering not only mechanical performances but also manufacturing limitations, with reasonable time and cost.

© 2021 China Ordnance Society. Publishing services by Elsevier B.V. on behalf of KeAi Communications Co. Ltd. This is an open access article under the CC BY-NC-ND license (<http://creativecommons.org/licenses/by-nc-nd/4.0/>).

1. Introduction

A penetrative projectile is designed to penetrate concrete structures and get activated inside the structure. Its key performance requirements needed to accomplish the purpose are impact resistance and explosive power. The impact resistance should be sufficient for penetration. As the projectile impacts the concrete structure, a large amount of kinetic energy is propagated to the projectile's materials as a shock wave. This shock wave is transferred to the energetic material inside the projectile, which increases the pressure of this material. If the pressure reaches the material's threshold pressure, then the projectile is ignited [1]. This causes activation of the projectile earlier than intended. Therefore, it is important to improve the impact resistance by lowering the

pressure of the energetic material. The second performance requirement, explosive power, is the amount of energy delivered to the exterior of the projectile when it is activated. A higher explosive power results in improved effectiveness of the projectile.

However, it is challenging to improve both performances because there is a trade-off between them. A conventional projectile carries energetic material inside a tube-shaped steel case, as depicted in Fig. 1. The steel case mainly contributes to the impact resistance and penetration depth, whereas the energetic material contributes to the explosive power. The energy propagated to the energetic material decreases as the thickness of the case increases, resulting in improvements in the impact resistance and penetration depth [2]. However, the explosive power decreases as the thickness increases; the increase in the volume of the case causes the amount of energetic material to decrease, thereby reducing the explosive energy. Additionally, a larger amount of explosive energy is consumed by the destruction of the thicker case, and hence, lesser energy is delivered to the outside of the projectile.

* Corresponding author.

E-mail address: thlee@hanyang.ac.kr (T.H. Lee).

Peer review under responsibility of China Ordnance Society

<https://doi.org/10.1016/j.dt.2021.05.001>

2214-9147/© 2021 China Ordnance Society. Publishing services by Elsevier B.V. on behalf of KeAi Communications Co. Ltd. This is an open access article under the CC BY-NC-ND license (<http://creativecommons.org/licenses/by-nc-nd/4.0/>).

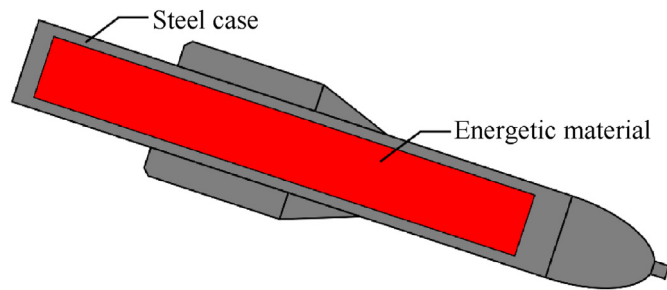


Fig. 1. Construction of conventional penetrative projectile.

To overcome this limitation, a new class of materials called reactive materials has been developed recently. Reactive materials are made of metallic compounds, exhibiting both high mechanical strength and high chemical energy [3]. Therefore, with regard to penetrative projectiles, the reactive material structure (RMS) can be utilized as a structural material as well as an energetic material. By contributing to both the impact resistance and explosive power of the projectile, an RMS can significantly improve the performance of a projectile in comparison with that of conventional ones without RMS [4]. RMSs are composed of intermetallic compounds, such as aluminum, nickel, magnesium, and zirconium.

However, owing to their high reactivities, it is difficult to manufacture reactive materials by conventional methods for processing alloys, which involve high temperature. Thus, alternative methods involving low temperature, such as cold gas dynamic spray (generally called cold spray), are used to process reactive materials [5–7]. Cold spray is suitable for the reactive material because it involves lower temperatures [8]. In the cold gas dynamic spray process, metallic powders, which make up the composition of the reactive material, are sprayed through a nozzle using a high velocity gas. As the sprayed particles impact the substrate with high velocity, they are bonded to the substrate and form an alloy [9,10]. Cold spray is employed in various applications, such as coating, repairing, and additive manufacturing [11,12]. Recently, cold spray has been widely used because of its advantages. Products with higher strength can be manufactured with lesser time and cost than that involved in other additive manufacturing processes. However, there are a few disadvantages of additive manufacturing by cold spraying. First, it is challenging to deposit powders in a narrow space because of the size of the spray nozzle. Because the RMS is located inside the steel case of the projectile, which has limited space, it is difficult to deposit the RMS directly in the case. Second, because the powders are sprayed, the geometry of the manufactured product exhibits high roughness and some unintended geometry. For example, when a cubical product is processed, the product has a trapezoidal cross-section rather than a rectangular one owing to particles sprayed to the product's side [13]. Therefore, it is challenging to fabricate structures with complex shapes. Typically, products undergo a machining or finishing process after the cold spray process [14]. Therefore, it is difficult to derive structural design of the RMS which satisfies manufacturing limitations of the cold spray.

In summary, because the RMSs are new components introduced in projectiles, design knowledge and experience of RMSs are unavailable. The determination of the shape and size of RMSs that maximize the performances of projectiles is necessary but challenging. Because penetration experiments of projectiles are time-consuming and extremely expensive, RMS design through repetitive experiments involves a lot of time, cost and inefficiency. Moreover, the producible shapes of RMS are limited owing to the characteristics of cold spray, such as deposition direction and

minimum thickness. These limitations hinder the determination of the shape and size of candidate designs.

In this study, design optimization of an RMS is performed for application to a penetrative projectile. First, a computational experiment of the penetration is performed to save time and cost of performance evaluation. Finite element models of the projectile and target are constructed, and the impact resistance of the projectile during penetration is assessed. The result of the finite element analysis is calibrated through comparison with a test result. Using the model, the shape of the RMS is determined through topology optimization. The performance requirement of the projectile and producible shape of the RMS are considered while formulating the topology optimization. Based on the optimal shape, detailed sizes of the RMS and steel case, including thickness and radius, are determined through size optimization, and hence, the optimal design of the RMS is achieved.

2. Review of literatures

Various researches have been studied on the reactive materials. However, although reactive materials have been developed for application to munitions, previous studies have mainly focused on the mechanical and chemical behavior of the materials. A few researchers have investigated the behavior of reactive materials as a component of projectiles. However, design of the reactive material structure has not been addressed. Lu et al. [15] addressed the behavior of reactive materials as projectiles, which impacts explosives. Xu et al. [16]. Investigated the damage to an aluminum plate target hit by a reactive material projectile. Kotei [17] examined the various mechanical behaviors of reactive materials. He tested the strength, sound speed, and fragmentation of reactive materials under the conditions encountered when they were applied to projectile casing. Although these studies considered projectile application, they mainly focused on the behavior of the projectile or target.

On the other hand, some researches address design problem of projectile. Graves et al. [18] designed the internal structure of a projectile case using topology optimization. However, the case was made of additively manufactured steel rather than reactive material. Although he adopted finite element analysis in the design procedure to save time and cost, a few limitations remain in the context of design optimization. The projectile was analyzed in linear static scheme rather than a non-linear dynamic one to save cost of the analyses. Furthermore, the topology optimization was performed by using a two-dimensional model rather than a three-dimensional model. However, because of these simplifications, it is difficult to accurately capture behavior of the projectile, and achievable design can be limited. Similarly, Provchy et al. [19] and Patel et al. [20] have performed topology optimization of inner structure of penetrative projectiles. However, both researches also simplified the analyses with two-dimensional static models. Therefore, they are difficult to capture behavior of the projectile in space. Additionally, only two-dimensional structures, which has lower degree of freedom in design, can be derived through the topology optimization. Meanwhile, some researchers have addressed external shape of the projectiles to improve aerodynamic performances. Liang et al. [21] have optimized canard profile of the projectile. Zhao et al. [22] have optimized geometry of tubular projectile to improve drag force characteristics. Kim [23] has optimized outer geometry of the projectile to improve range. Contrary to this paper, these researches are focused on the aerodynamic performances. Aerodynamic performances are assessed through computational fluid dynamics (CFD), and size optimization is considered rather than topology optimization.

In summary, studies on the reactive material are focused on

their mechanical and chemical behavior rather than design application problem. Therefore, design problem of the RMS has not been addressed yet. On the other hand, some researchers addressed topology optimization problem of projectile structure. However, material of the structure is limited to steel rather than the RMS, and penetration analysis and optimization are performed with two-dimensional simplification. The researches address aerodynamic performances are based on the CFD rather than penetration analysis, and only geometric parameters are considered during optimization. Therefore, a new research addresses topology optimization of the RMS based on three-dimensional penetration analysis is required.

3. Design optimization methods and results

3.1. Finite element analysis of penetration test

It is necessary to assess the projectile performance with respect to the variation in the RMS design, to perform design optimization of the RMS for maximizing the projectile's performance. The impact resistance of the projectile can be evaluated through a penetration test. However, a penetration test incurs high costs and is time-consuming. This limits the application of the test in design optimization, which requires dozens or hundreds of repetitive performance evaluations. Moreover, the impact resistance should be quantified by the pressure of the energetic material. However, it is challenging to measure the maximum pressure of the energetic material through the penetration test.

To resolve these problems, finite element analysis of the penetration test is employed in this study. A finite element model comprising the projectile and target is constructed based on the penetration test. The geometry, material properties, and boundary conditions of the test are implemented in the model. The model is calibrated with the test result by comparing the residual velocity of the projectile after penetrating the target. The impact resistance of the projectile, which is the maximum pressure of the energetic material, is assessed using the model.

3.1.1. Finite element modeling

The finite element model is constructed in LS-DYNA based on the penetration test. Fig. 2 illustrates the projectile used in the test and its schematic. Considering confidentiality, the dimensions in the illustration are normalized and the units have been omitted. In the test, the projectile is launched by an air gun, and then penetrates a concrete target. Initial and residual velocity of the projectile are measured before and after penetration, respectively. The velocity is measured by using high speed camera. Fig. 3 depicts the target in the test setup. The finite elements are generated as depicted in Fig. 4 based on the dimensions of the projectile and target. Solid elements are used for both the projectile and target models. Hexahedron elements with 8 nodes are used in the target. Whereas in the projectile, pentahedron elements with 6 nodes are

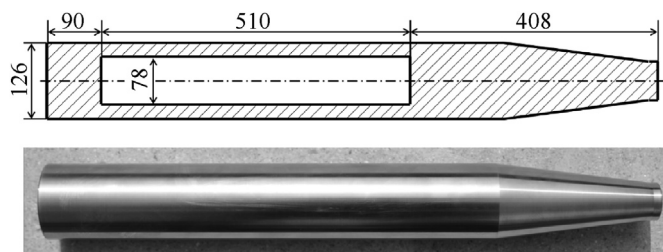


Fig. 2. Projectile used in the test and its dimensions.



Fig. 3. Target of the penetration test.

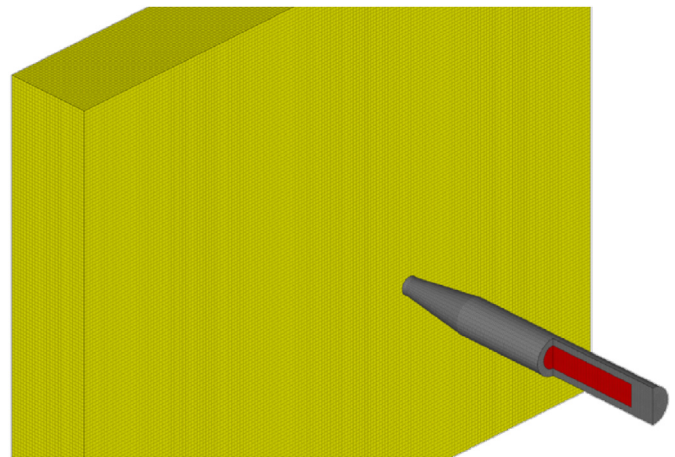


Fig. 4. Finite element model of projectile and target.

used with the hexahedron elements.

Material properties are assigned to the elements according to the materials used in the test. The target is made of reinforced concrete. There are a number of material models for concrete, such as continuous surface cap model (CSCM) [24,25], Johnson–Holmquist damage model [26], and Karagozian & Case concrete model [27,28]. CSCM is employed in this study because it is developed for high dynamic loadings [29], and this study addresses similar loads. In LS-DYNA, CSCM is implemented as material model 159. Density and unconfined compression strength parameters are assigned to the model, as listed in Table 1. Additionally, the element erosion option is assigned to the concrete elements to express failure during impact. The erosion criterion is defined by the maximum principal strain, which is the MXEPS variable of MAT_ADD_EROSION in LS-DYNA. The maximum principal strain is determined by calibration, as described in Section 3.1.2.

The projectile comprises a steel case, an energetic material, and an RMS. The simplified Johnson–Cook model is employed in the steel case to consider the strain rate effect that occurs during impact. Johnson–Cook model [30] is suitable for metallic materials whose strain rates vary over a wide range [31], and hence, is suitable for application here because the steel case exhibits wide variations in the strain rate because of high velocity impact. The model employed in this study is a simplified variant of the generic

Table 1
Parameters assigned in the finite element model.

Material	Material model	Parameter	Assigned value	Unit
Concrete	CSCM	Density	2390	kg · m ⁻³
		Unconfined compression strength	46.91	MPa
Steel (case)	Simplified Johnson–Cook	Density	7850	kg · m ⁻³
		Young's modulus	206.9	GPa
		Poisson's ratio	0.3	–
		A	1200	MPa
		B	808	MPa
		C	0.031	–
		n	0.4543	–
Energetic material	Null	Density	1775	kg · m ⁻³
		Young's modulus	3780	MPa
		Poisson's ratio	0.3	–
	Gruneisen EOS	C	2.105	km · s ⁻¹
		S ₁	2.144	–
		γ ₀	0.9902	–
Reactive material	Piecewise linear plasticity	Density	3460	kg · m ⁻³
		Young's modulus	161.5	GPa
		Poisson's ratio	0.3	–

Johnson–Cook model, wherein the thermal effect and damage are omitted [32]. The simplified model is 50% faster than the generic one [33], thereby saving computational time and cost. Because our focus is on the behavior of the energetic material rather than on the steel case, the simplified model is employed for computational efficiency. It is implemented as material model 98 in LS-DYNA, and the flow stress in the model can be expressed as follows:

$$\sigma_y = (A + B\bar{\epsilon}^n)(1 + C \ln \dot{\epsilon}^*) \quad (1)$$

where $\bar{\epsilon}^p$ and $\dot{\epsilon}^*$ are the effective plastic strain and normalized effective strain rate, respectively. A , B , C , and n are model constants. The material properties and constants assigned to the model are listed in Table 1.

The energetic material is modeled using an equation of state (EOS) to capture pressure of the material that is formed by the shock wave. The Gruneisen EOS, which is widely used for shock-compressed solids, is employed [34,35]. It is implemented as EOS form 4 in LS-DYNA, and calculates the pressure of the compressed and expanded materials by the following equation [32]:

$$P_{\text{compressed}} = \frac{\rho_0 C^2 \mu \left[1 + (1 - \gamma_0/2)\mu - a/2\mu^2 \right]}{\left[1 - (S_1 - 1)\mu - S_2\mu^2/\mu + 1 - S_3\mu^3/(\mu + 1)^2 \right]^2} + (\gamma_0 + a\mu)E \quad (2)$$

$$P_{\text{expanded}} = \rho_0 C^2 \mu + (\gamma_0 + a\mu)E$$

$$\text{where } \mu = \frac{\rho}{\rho_0} - 1$$

where C is the bulk speed of sound, ρ_0 is the initial density, ρ is the current density, and γ_0 is Gruneisen gamma. S_1 , S_2 , and S_3 are coefficients expressing dv_s/dv_p , i.e., the slope of the cubic shock-velocity vs. particle-velocity curve. a is the first-order volume correction coefficient. Density, Young's modulus, and Poisson's ratio are assigned using the null material model (material model 9). The assigned values of the material properties and constants are listed in Table 1.

Development of reactive materials is still at an early stage, and finite element analysis of reactive materials has not been studied

yet. It is challenging to select a suitable model for a reactive material from among the material models developed. In this study, a piecewise linear material model with strain rate effect is employed to model a reactive material without assumption. The model can express plastic behavior based on experimental data, and tabular data of stress–strain curve can be defined for various strain rates. Therefore, the model is suitable in our study, where prior knowledge of the material is insufficient and the strain rate varies over a wide range. The model is implemented as material model 24 in LS-DYNA. The stress–strain data of the reactive material Ni₆₃Al₃₂Cu₅ is assigned to the model [36]. Stress–strain curves for plastic deformation are assigned for six strain rates from $1 \times 10^{-3} \text{ s}^{-1}$ to $5 \times 10^3 \text{ s}^{-1}$, based on the data. Other material properties such as density, Young's modulus, and Poisson's ratio are listed in Table 1.

Next, a boundary condition is imposed on each component. For the concrete target, the constraint is imposed on the four sides that are parallel to the projectile's direction. Displacements of all the nodes on the sides are constrained in six degrees of freedom. For the projectile, initial velocity is assigned as with the test. A velocity of 244 m/s is imposed on the projectile's components, namely, the steel case, energetic material, and RMS. Additionally, an eroding surface-to-surface contact is imposed between the target and steel case to make the projectile impact the target. The concrete target is assigned to the master contact segment, and the steel case is assigned to the slave contact segment.

3.1.2. Results and calibration

The finite element model is analyzed using massively parallel processing (MPP) in LS-DYNA. Two Intel Xeon E5-2697 v3 processors and two Intel Xeon E5-2695 v4 processors are used in the analysis. In total, 64 cores are employed. In the calibration procedure, the model is analyzed for 0.003s to make the projectile penetrate the target thoroughly. The maximum principal strain for element erosion of the concrete target is calibrated by comparing the projectile's residual velocities of the test and analysis. The residual velocity is the velocity of the projectile after penetration. Before penetration, the projectile possesses its initial velocity and corresponding kinetic energy. A part of the kinetic energy is used to damage the target and projectile itself during the penetration process. After penetration, the remaining energy remains in the projectile as kinetic energy, which is proportional to the residual velocity. Therefore, the amount of energy used for the penetration can be calibrated using the residual velocity. Moreover, because the residual velocity can be easily measured in the test, it is the most

suitable measure of the model calibration available. In the test, the initial velocity of the projectile is 244 m/s, and residual velocity is 217 m/s. The maximum principal strain is increased from the initial value, 0.14, and the change in the residual velocity is observed. Table 2 presents the maximum principal strain values and the corresponding residual velocities. As the maximum principal strain increases, elements of the concrete target erode at higher principal strain. Therefore, more kinetic energy of the projectile is consumed to deform the elements of the target, resulting in a decrease in the residual velocity. In accordance with the result, the maximum principal strain for element erosion is calibrated to 0.22, with least error in the residual velocity.

The impact resistance of the base projectile model, which is modeled without RMS, is assessed using the calibrated parameter. Fig. 5 depicts the penetrated concrete targets of the test and analysis. The holes caused by the penetration exhibit similar size and shape. In the test, some of the concrete surrounding the hole is spalled from the rear side of the target. In the analysis, this spalling is not observed from the rear. However, it can be observed in a cross-sectional view. The vertical spalling diameters of the test and analysis are also similar. However, radial cracks in the target are observed in the test, whereas they are not apparent in the analysis. The cracks can be captured by improving the analysis model, such as by reducing the mesh size and applying a nonlocal model [37]. However, such improvements cause an increase in the computational resource requirement. Moreover, they capture the behavior of the target rather than that of the projectile, whereas our focus is on the impact resistance of the projectile. Therefore, further improvements in the concrete model are not considered in this study.

Fig. 6 illustrates the pressure distribution of the energetic material in the projectile. It is verified that a shock wave occurs as the projectile impacts the target, and the shock wave propagates back and forth in the projectile. A projectile with the initial design, which does not incorporate RMS, is assessed to serve as a reference for impact resistance. The maximum pressure of the energetic material, which is a measure of the impact resistance, is 8.69 kbar in the initial design. Additionally, analysis time of the model is reduced to decrease the computational resource requirement for design optimization. During the calibration, the analysis is performed until the projectile penetrates the target thoroughly, to measure the residual velocity. On the other hand, in design optimization, performance which will be assessed is the maximum pressure. Therefore, the analysis time is limited to the period wherein the maximum pressure occurs, thereby reducing the analysis time from 0.003 s to 0.0005 s. As a result, approximately 10 min of computational time is consumed for an analysis.

3.2. Topology optimization

There are challenges in the determination of the RMS shape for a penetrative projectile. Because the design of the RMS has not been studied, prior design knowledge or experience of the RMS for penetrative projectiles are unavailable. Therefore, it is challenging to determine the effective shape of the RMS for improving the projectile's impact resistance. Moreover, the producible shapes of

Table 2
Maximum principal strain and residual velocity.

Maximum principal strain	Residual velocity (m·s ⁻¹)	Relative error (%)
0.14	220.90	1.80
0.18	219.92	1.35
0.21	218.52	0.70
0.22	217.95	0.44
0.23	215.92	0.50

the RMS are limited because of its manufacturing method, i.e., cold gas dynamic spray, thereby hindering the development of candidate designs in the design process.

In this study, to resolve these challenges, a topology optimization is employed to determine the RMS shape. Topology optimization is one of the most effective design methods for determining the initial shape of a structure without prior knowledge, experience, or design. Therefore, it is suitable for the RMS, where no prior design experience exists. Manufacturing constraints of the RMS are collected and considered in the topology optimization formulation such as design variables and constraints of the optimization. Topology optimization is performed based on analysis results of the finite element analysis presented in Section 3.1. The optimal shape of the RMS, which maximizes the impact resistance of the projectile, is derived within the design space inside the steel case.

The design space for the RMS is depicted in Fig. 7. With the introduction of the RMS, the projectile comprises the steel case, RMS, and energetic material. The RMS is designed in the free space inside the steel case, and the energetic material is filled in the remaining free space. The shape is assumed to be constant along the axial direction of the projectile, and the shape of the cross-section is determined. Without the RMS, the steel case is the only structural component of the projectile. However, when the RMS is introduced, the RMS also functions as a structural component. Therefore, the thickness of the steel case should be decreased when the RMS is introduced. The thickness of the steel case in Fig. 7 is less than that of the projectile without the RMS (which is depicted in Fig. 2) by 37.5%. After topology optimization, the specific value of the case thickness is determined through the size optimization process described in Section 3.3.

3.2.1. Manufacturing constraints of RMS

As aforementioned in introduction, reactive materials are manufactured by cold spray process because of their high reactivity. Shapes of the RMS, which can be manufactured by the cold spray, are limited compared to the conventional manufacturing processes. According to the limitations presented in introduction, the producible shapes of RMSs are constrained as follows:

- All the parts of the RMS should be connected to each other.
- The RMS should be in contact with the steel case.
- The shape should consist of a tube and plate.

Because the RMS cannot be deposited directly inside the steel case, the RMS must be processed independently outside the case, and then fitted inside the case. Otherwise, the RMS cannot be constrained in the case because the energetic material is not a solid structure and does not have enough mechanical strength necessary for constraint of the RMS. The first and second manufacturing constraints are geometrical interpretations of the installation limitation. If the two conditions are satisfied, the RMS can be fitted inside the steel case. In the third constraint, the shapes of the RMS are limited to simple ones, considering the challenges in processing complex shapes. Moreover, unlike for other alloys, it is challenging to machine a reactive material because of its reactivity. Therefore, the shape of the RMS is limited to the simplest ones, such as those consisting of a tube and plate, which are easy to be deposited.

Fig. 8 depicts cross-sections of candidate shapes of the RMS. The gray, green, and red sections represent the steel case, RMS, and energetic material, respectively. In the figure, (a) and (b) represent shapes which can be manufactured, whereas (c) and (d) represent shapes which cannot be manufactured. The shapes illustrated in (a) and (b) satisfy the manufacturing constraints. They consist of a tube and plate and can be fitted inside the case. Meanwhile, the shapes depicted in (c) and (d) do not satisfy the constraints. For example,



Fig. 5. Damage of targets of the test (left) and analysis (right).

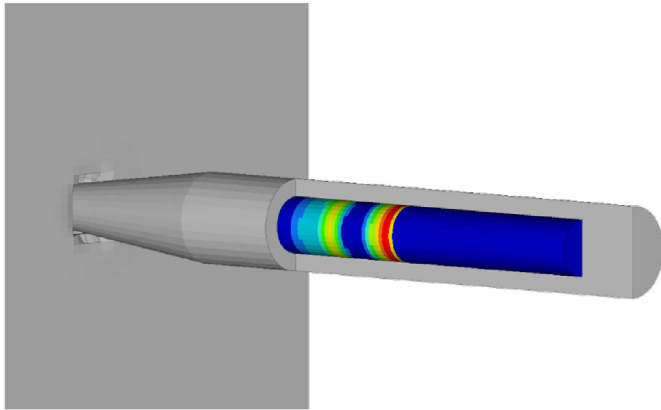


Fig. 6. Pressure distribution of energetic material.

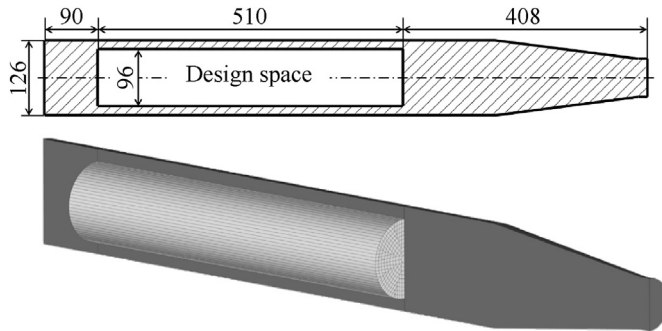


Fig. 7. Design space for topology optimization.

(c) consists of plates, and all the parts of the RMS are connected to a piece. However, because they are not in contact with the case, they cannot be constrained by it. Similarly, (d) consists of plates that are in contact with the case. However, it cannot be constrained because the RMS is disconnected. The three manufacturing constraints described above are considered in the topology optimization formulation to derive the producible shapes.

3.2.2. Optimization method and definition of design variables

A typical topology optimization problem is formulated as follows [38]:

$$\min_{\rho} F(u(\rho), \rho) \quad (3)$$

$$\text{s.t. } G_0(\rho) = \int_{\Omega} \rho dV - V_0 \leq 0$$

$$G_j(u(\rho), \rho) \leq 0 \text{ for } j = 1, \dots, m$$

ρ represents the material density of each element in the design domain. The density is a continuous variable between zero and one; zero indicates the absence of the material, and one indicates its presence. The shape of the structure can be expressed by the distribution of the material density, and the topology of the structure is determined by the optimal density. F and G_j represent the objective function and constraints of the optimization, respectively. G_0 is the volume fraction constraint, which limits the maximum volume of the optimal structure. The typical methods addressing a linear static structure solve the problem by using gradient information of the objective function and constraints, and sensitivity analysis is necessary to derive the gradient information.

However, it is challenging to employ conventional topology optimization methods, such as solid isotropic material with penalization method [39] and level set method [40], for the topology optimization of the RMS. First, the design space where the RMS is not distributed should be filled with the energetic material, i.e., the design space should be completely filled with the RMS and energetic material. However, in conventional methods, a design space with zero material density remains a void. Second, sensitivity analysis of the objective function and constraint cannot be performed. Because the finite element analysis described in Section 3.1 is a non-linear dynamic analysis, which involves time-dependent explicit calculation, it is difficult to take derivatives of the performance functions. Therefore, the topology optimization of a non-linear dynamic structure employs alternative methods, such as equivalent static load method [41] or discrete optimization algorithms. The equivalent static load method imposes a static load on a structure, which is equivalent to a dynamic load. However, it is not suitable in our study, where the maximum peak pressure of the energetic material needs to be assessed. It is infeasible to assess the maximum pressure by using static analysis.

Meanwhile, methods employing discrete optimization algorithms define the presence of each element by using discrete variables that are expressed by zero or one. The discrete variable can represent an element as well as a substructure with specific shape, such as a truss and plate. Kawamura et al. employed the genetic algorithm (GA) [42] in truss topology optimization [43]. Luh et al. employed the particle swarm optimization (PSO) algorithm [44] by using discrete variables representing the presence of elements [45]. Fang et al. employed the artificial bee colony (ABC) algorithm [46] in the topology optimization of multicell tubes [47]. These methods can be employed in our study. First, because the design variable is

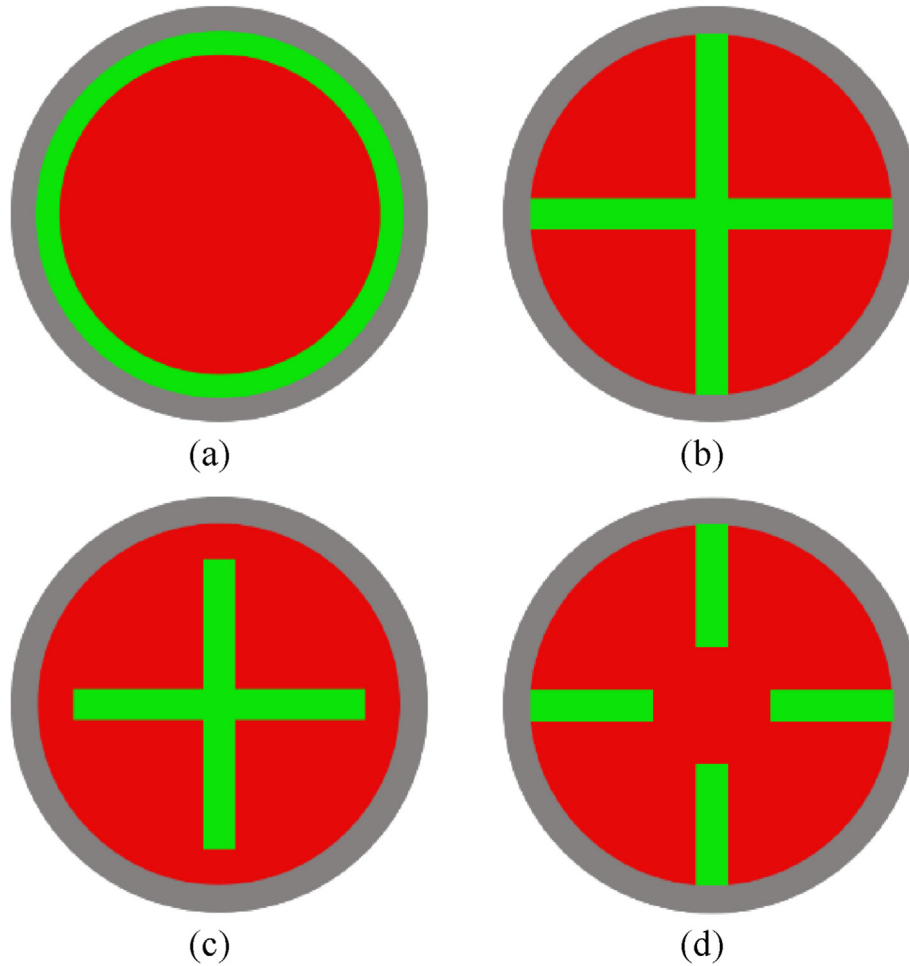


Fig. 8. Example shapes of manufacturing constraint.

binary, it is convenient to modify the algorithm to fill the void design space with the energetic material, e.g., applying one and zero for the reactive material and energetic material, respectively. Second, because the methods do not require sensitivity information, they can incorporate non-linear dynamic analysis. Therefore, in this study, a discrete optimization algorithm is employed in the topology optimization. The ABC algorithm is employed because it exhibits better performance in comparison with GA or PSO [47,48].

In accordance with the optimization method, the discrete design variable for the topology optimization is defined. Because the producible shapes of the RMS are limited, i.e., to tube and plate, the design variable is defined to represent candidate shapes of the structure rather than an element. Fig. 9 illustrates the candidate shapes represented by the variables. Fig. 9 depicts a quarter of the cross-section of the projectile's finite element model. The gray section represents the steel case; the white section represents the design space, which would be filled with the RMS and energetic material; and the green lines represent the shape of the candidate structures. The mesh is constructed with four-fold rotational symmetry, and the other three-quarters are identical to those in Fig. 9.

According to the third manufacturing constraint, tube- and plate-shaped candidate structures are defined using finite elements. Fig. 9 (a) depicts tube structures with various radii. Ten candidate tube structures are defined. The number of tube structures is limited to one or two considering the volume of the

energetic material. If three or more tube structures exist, the volume for the energetic material will be insufficient. This results in violation of the volume constraint, which is described in Section 3.2.3. Ten candidate tube structures are assigned to the design variables $\rho_1 \sim \rho_{10}$. Fig. 9 (b) depicts the plate structures that are located inside the inner tube structure, to which the design variables $\rho_{11} \sim \rho_{12}$ are assigned. Two structures are defined according to the shape of the mesh. Fig. 9 (c) depicts the plate structures that are located between the inner and outer tube structures, to which the variables $\rho_{13} \sim \rho_{27}$ are assigned. Finally, Fig. 9 (d) depicts the plate structures that are located outside the outer tube structure, to which the variables $\rho_{28} \sim \rho_{44}$ are assigned. Thus, 44 design variables that configure the design of the RMS are defined. All the design variables are binary, which are expressed as zero or one. Zero and one represent absence and presence, respectively, of the candidate RMS.

Fig. 10 illustrates examples of the RMS design configured using the defined design variables. The green and red elements represent the RMS and energetic material, respectively. Among the 44 design variables, $\rho_5, \rho_8, \rho_{11}, \rho_{20}, \rho_{30},$ and ρ_{42} are defined as one. The other 38 variables are defined as zero. Shapes of individual candidate structures are expressed on the left side in Fig. 10. A candidate RMS design is configured by combining the shapes, as depicted on the right side in Fig. 10. According to the definitions of the variables, the plate structures are bounded by the tube structures. For example, the plate structure defined by ρ_{11} spans across the radial direction.

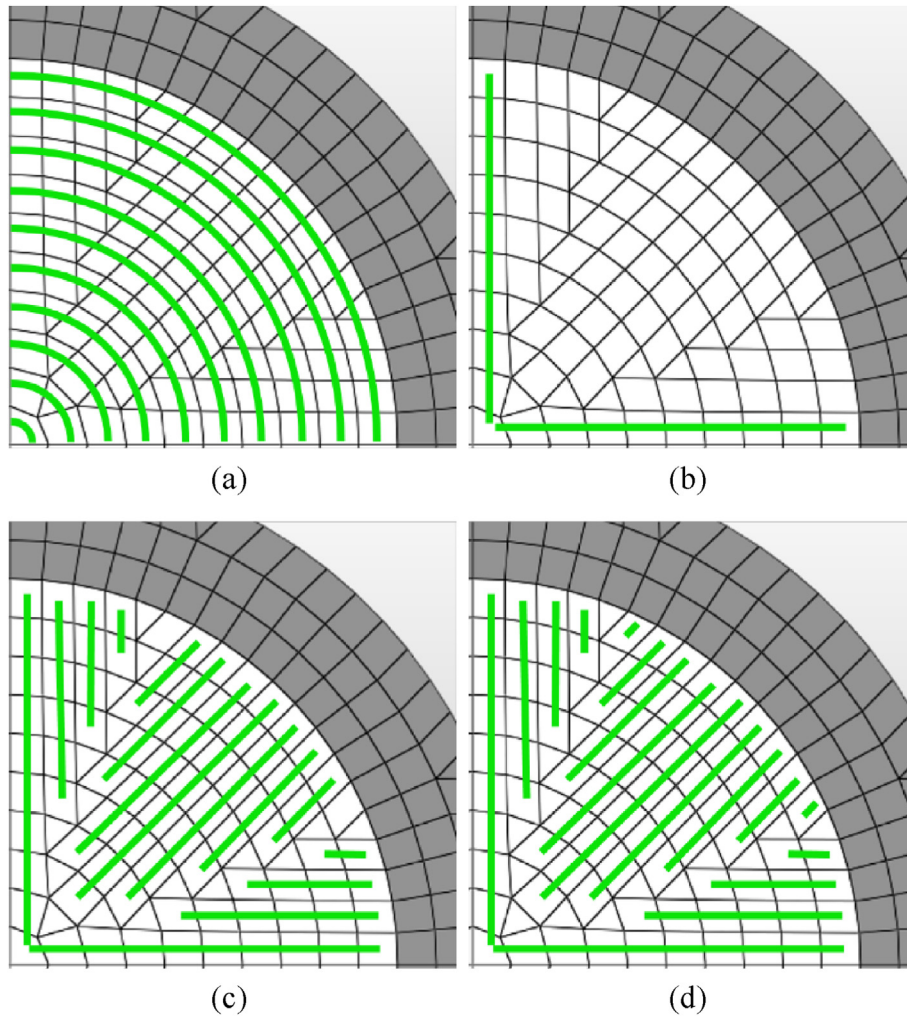


Fig. 9. Definition of design variables for topology optimization.

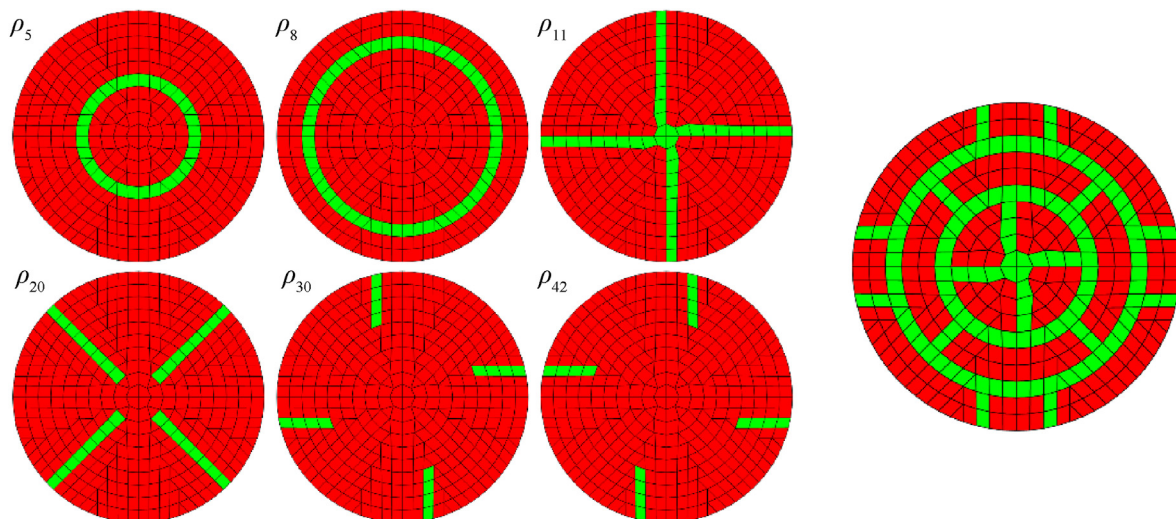


Fig. 10. Example shapes of the RMS that define the variables.

However, in the RMS design, the structure is bounded within the tube structure, which is defined by ρ_5 . This is because ρ_{11} is defined as being located inside the inner tube structure. Similarly, the plate structures defined by ρ_{20} , ρ_{30} , and ρ_{42} are bounded by the tube structure according to their definitions.

The candidate RMS designs configured by the design variables are applied to the finite element model to assess the performance of the design. Modification of the finite element model is performed by assigning the material models to the finite elements of the design space. The reactive material model is assigned to the finite elements that are defined as the RMS. Similarly, the energetic material model is assigned to the remaining elements of the design space.

3.2.3. Optimization formulation

The topology optimization is formulated as the following equation:

$$\min_{\rho} P_{\max}(\rho) \quad (4)$$

$$\begin{aligned} \text{s.t.} \quad & V_{EM}^{LB} - V_{EM}(\rho) \leq 0 \\ & \sum_{i=1}^{10} \rho_i - 2 \leq 0 \\ & 1 - \rho_{10} - \sum_{i=28}^{44} \rho_i \leq 0 \\ & n_{RMS} - 1 = 0 \end{aligned}$$

$$\text{where} \quad \rho_i \in [0, 1], \quad i = 1, \dots, 44$$

ρ represents the 44 design variables defined above, which are binary variables expressed as zero or one. The objective function is configured to maximize the impact resistance of the projectile, i.e., to minimize the maximum pressure of the energetic material. P_{\max} assessed by finite element analysis represents the maximum peak pressure of the energetic material during penetration. The first constraint limits the minimum volume of the energetic material. V_{EM}^{LB} represents the volume of the energetic material of the base projectile model, which is designed without the RMS. Because the explosive power of the projectile is proportional to the volume, the volume is formulated and assessed in the optimization. The RMS and energetic material are enclosed in design space as shown in Fig. 7. The volume is assessed by multiplying longitudinal length of the design space to area of energetic material on cross-section. The second constraint represents the limitation in the maximum number of tube structures. As mentioned above, the maximum number is limited to two because three or more tube structures result in the violation of the first constraint. The third constraint represents the manufacturing constraint, i.e., the contact between the RMS and steel case. As mentioned in Section 3.2.1, the RMS should be in contact with the steel case in which it is installed. The structures defined by ρ_{10} and $\rho_{28} \sim \rho_{44}$ are located at the outermost portion of the design space, and are in contact with the steel case. Therefore, the third constraint is defined to ensure that at least one of these structures is present in the design. The last constraint also represents the manufacturing constraint, connectivity of the RMS. All the parts of the RMS should be connected together as one to be fitted inside the steel case. Therefore, the number of disconnected RMS, n_{RMS} , is assessed and limited to one.

3.2.4. Results

The topology optimization of the RMS is performed based on the optimization method, design variables, and formulation. The ABC

algorithm presented by Fang et al. [46] is implemented in MATLAB. The variation in the design variables is implemented in the finite element model by modifying the LS-DYNA keyword file from MATLAB. The RMS or energetic material model is assigned to each element according to the design variables. The maximum pressure of the energetic material is assessed by executing LS-DYNA from MATLAB. The result is extracted by executing the LS-PrePost script. The population size and maximum number of generations are configured as 5 and 24, respectively.

The topology optimization result is depicted on the left side in Fig. 11. Among the 44 design variables, 6 ($\rho_4, \rho_8, \rho_{11}, \rho_{13}, \rho_{28}$, and ρ_{36}) converge to 1. The remaining design variables converge to zero. The optimization history is depicted in Fig. 12. The best design is obtained at the sixth generation. The objective function and constraints of the optimal topology are presented in Table 3. The objective function (the maximum pressure of the energetic material) is 3.12 kbar, which is lesser than that of the base model without RMS by 64%. The optimal topology satisfies all the constraints of the formulation. The volume of the energetic material satisfies its lower boundary. Furthermore, all the geometric constraints, which are related to the manufacturing constraints, are satisfied. According to the definition of the design variables, the optimal RMS consists of producible shapes, i.e., tube- and plate-shaped structures. The other manufacturing constraints of the RMS are also satisfied. As depicted in Fig. 11, all the parts of the RMS are inter-connected, and the RMS is in contact with the steel case. Therefore, the optimal RMS can be fitted inside the steel case, and all the manufacturing constraints configured in Section 3.2.1 are satisfied.

However, because of the shape of the finite elements, the plate structures of the optimal shape do not exhibit a perfect plate shape. Therefore, the optimal RMS shape derived from the topology optimization is smoothed, as depicted on the right side of Fig. 11. A few plate structures with trapezoidal cross-sections are smoothed such that they exhibit a square cross-section. The impact resistance and energetic material volume are assessed using the smoothed shape, and the results are presented in Table 3. The maximum pressure of the energetic material is increased from 3.12 kbar to 3.46 kbar. However, it is 60% lower than that of the base model. The volume of the energetic material satisfies the constraint, and increases as a few trapezoidal elements are modified to become square elements. As a result, the shape of the RMS that maximizes the impact resistance and satisfies the manufacturing constraints is determined.

3.3. Size optimization

In Section 3.2, the optimal shape of the RMS determined through topology optimization, and the smoothed shape is assessed. Both the shapes exhibit substantial improvement in impact resistance, while satisfying the manufacturing constraints of the RMS. However, the dimensions of the RMS, such as thickness and radius, are not addressed in the topology optimization. Additionally, in topology optimization, the thickness of the steel case is reduced arbitrarily in comparison with the base model, to achieve design space for the RMS. Therefore, in this section, the dimensions of the RMS and steel case are optimized through size optimization. As well as the maximum pressure of the energetic material, tangential stress of the steel case is assessed to achieve structural safety of the steel case. First, the optimization formulation is configured by defining the geometric design variables, objective function, and constraints. Second, a kriging model, a mathematical surrogate model, is introduced for efficient size optimization, and the models are constructed for the projectile performances. Finally, size optimization is performed based on the kriging models to determine the final design of the projectile.

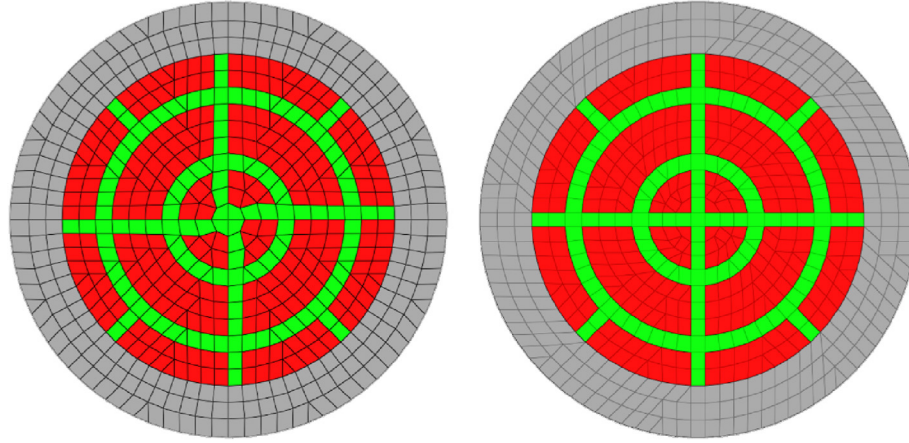


Fig. 11. Cross-section of optimal and smoothed shape of RMS.

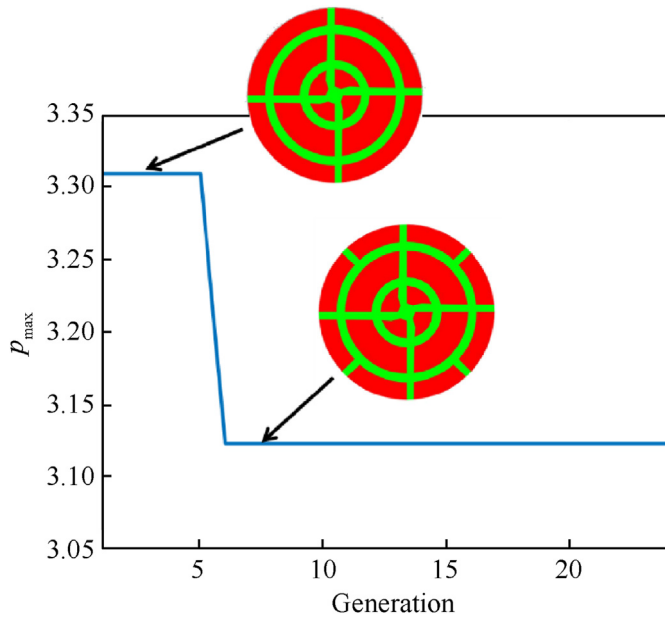


Fig. 12. History of the topology optimization.

3.3.1. Optimization formulation

The design variables for the size optimization are configured as depicted in Fig. 13. Dimensions, such as radius and thickness, of the smoothed shape are selected as the design variables. The inner radius of the steel case is also selected as a variable. As mentioned in Section 3.2, the thickness of the steel case is arbitrarily reduced

from that of the base model, i.e., by 37.5%, to achieve design space for the RMS. Therefore, a quantitative assessment of the thickness, which is a function of the inner radius, should be conducted as part of the size optimization process. Therefore, nine design variables, which are continuous variables, are selected for the size optimization. Their boundaries are presented in Table 4. As mentioned above, the values in the table are normalized, and the units are omitted considering confidentiality. Nevertheless, they are consistent with the dimensions denoted in Figs. 2 and 7.

The size optimization is formulated based on the formulation of the topology optimization. As with the topology optimization, the most important performance measure to be maximized is the impact resistance of the projectile, which can be varied by altering the dimensions of the RMS and steel case. From among the constraints of the topology optimization, the volume constraint of the energetic material, which represents the explosive power, should be considered in the size optimization as well. This is because the volume varies according to the variations in the dimensions. Meanwhile, the second to fourth constraints, which are formulated for the manufacturing constraints of the RMS, need not be considered in the size optimization. Because variations in the dimensions do not affect the manufacturing constraints, i.e., the shape of the RMS and the contact between the RMS and steel case. Therefore, the size optimization is formulated as the following equation:

$$\min_{\mathbf{x}} P_{\max}(\mathbf{x}) \quad (5)$$

Table 3
Performances of the optimal and smoothed shapes.

	Function	Formulation	Base model	Optimal shape	Smoothed shape	Unit
Objective function	$P_{\max}(\rho)$	Minimize	8.69	3.12	3.46	kbar
Constraint	$V_{EM}(\rho)$	$\geq 2.437e6$	2.437e6	2.473e6	2.492e6	—
	$\sum_{i=1}^{10} \rho_i$	≤ 2	—	2	2	—
	$\rho_{10} + \sum_{i=28}^{44} \rho_i$	≥ 1	—	2	2	—
	n_{RMS}	$= 1$	—	1	1	—

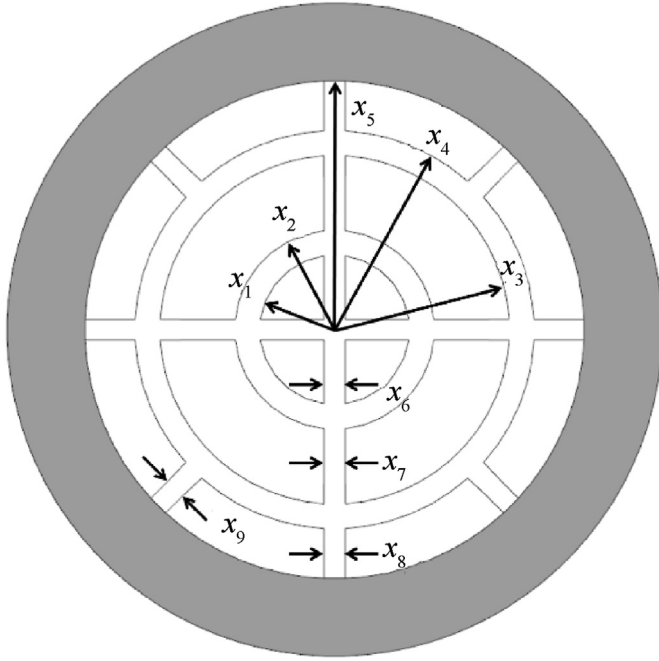


Fig. 13. Design variables of size optimization.

Table 4
Lower boundary, upper boundary, and optimal design of the variables.

Design variable	Lower boundary	Upper boundary	Optimal design
x_1	11.40	16.20	15.63
x_2	17.40	22.20	17.61
x_3	30.60	35.40	30.98
x_4	36.60	41.40	37.58
x_5	45.00	51.00	48.48
x_6	0.99	6.99	4.42
x_7	0.99	6.99	1.73
x_8	0.99	6.99	2.48
x_9	0.99	6.99	5.49

$$\begin{aligned}
 \text{s.t. } & V_{EM}^{LB} - V_{EM}(\mathbf{x}) \leq 0 \\
 & \sigma_{case} - \sigma_{case}^{UB} \leq 0 \\
 & x_i^{LB} \leq x_i \leq x_i^{UB}, \quad i = 1, \dots, 9
 \end{aligned}$$

\mathbf{x} which is bounded by its lower and upper boundaries represents the vector of nine design variables. As described above, the maximum pressure and volume of the energetic material are configured as the objective function and constraint, respectively. Additionally, σ_{case} in the second constraint represents the maximum tangential stress of the steel case during penetration. It is constrained to be less than that of the base model, σ_{case}^{UB} , to achieve structural safety of the steel case considering the variation in the thickness of the case. Among the tangential, radial, and axial stresses of the steel case, the axial stress is the largest. However, it decreases as the thickness of the steel case decreases because of the decrease in kinetic energy caused by the reduction in projectile weight. Therefore, it is not a suitable measure for determining the thickness of the steel case. The radial stress does not exhibit significant dependence on the thickness. Meanwhile, the tangential stress increases as the thickness decreases. This is because the case is subjected to a radial force from the inside, which is caused by the pressure of the energetic material. Therefore, the tangential stress is selected as the measure of structural safety.

3.3.2. Kriging surrogate model

The penetration analysis takes dozens of minutes for a single analysis, and dozens or hundreds of analyses are necessary for the optimization. Therefore, a lot of computational cost is incurred when the optimization is performed based on the response from the analysis. Therefore, in the size optimization, a kriging surrogate model is employed to save computational cost and improve efficiency. The kriging surrogate models, which predict maximum pressure and maximum tangential stress, are constructed based on the finite element analyses. The kriging models are employed to assess the performances during optimization process. The kriging surrogate model is a mathematical model that predicts the response of a black-box function based on given information, i.e., sample points [49]. Typically, it is challenging for surrogate models to predict the response of discrete input variables. Therefore, it is not considered in the topology optimization, where the variables are binary. However, it is considered in the size optimization where the design variables are continuous. The sample points for the kriging model are determined by optimal Latin-hypercube design (OLHD) [50] and maximin distance design (MDD) [51]. For nine design variables, 55 sample points are determined by OLHD and an additional 249 by MDD, within the design boundary. Therefore, the penetration analysis is performed for 304 sample points. The variations in the design variables of the sample points are applied to the finite element model by morphing. The coordinates of the nodes in the LS-DYNA keyword file are modified according to the variations in the dimensions. The maximum pressure of the energetic material and maximum tangential stress of the case are assessed for each sample point.

Kriging surrogate models are constructed for the two performances of the projectile, i.e., the maximum pressure of the energetic material and the maximum tangential stress of the case, by using the sample points. Zeroth-order polynomial and Gaussian correlation function are employed for the regression model and correlation model, respectively, of the kriging model. The constructed models are validated using the leave-one-out cross-validation method, which does not require additional sample points for validation [52]. The accuracy of the model is assessed by root-mean-square error, which is normalized by the difference between the maximum and minimum responses of the sample points. As a result, the model of maximum pressure exhibits an error of 17.58%, and the model of maximum stress exhibits an error of 16.84%. Because the penetration analysis exhibits high non-linearity and the performances are the maximum peak values of the time-series response, it is challenging to reduce the errors in the kriging models further. Although the models exhibit certain errors, the trends between the design variables and performances can be captured through the models.

Fig. 14 depicts the constructed kriging models, and the performances are plotted with respect to the design variables x_6 and x_7 . As provided in Fig. 13, x_6 and x_7 represent thicknesses of the plate structures located at inner and middle of the RMS, respectively. In case of the maximum pressure, both thicknesses have quadratic relationship with the pressure rather than linear one. Therefore, it can be inferred that the pressure has nonlinear behavior with respect to the geometric dimensions. On the other hand, x_6 has little effect on the maximum tangential stress, while x_7 has much more effect. It can be interpreted intuitively that the distance between each structure and steel case affects the degree of effect. Because the structure of x_6 is located far from the steel case, it must have little effect on the stress of case. Therefore, it can be confirmed that the kriging models well express physical relations between variables and performances.

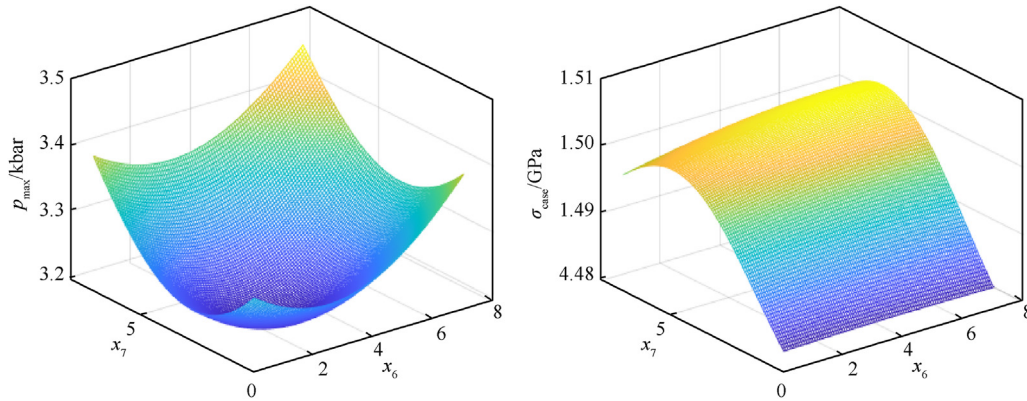


Fig. 14. Kriging models of the performances.

3.3.3. Results

The size optimization of the RMS and steel case is performed based on the optimization formulation of Eq. (5). Gradient-based optimization, a sequential quadratic programming algorithm [53] that is implemented in MATLAB, is employed to solve the problem. The middle values of the upper and lower boundaries, $x_i^{LB} + x_i^{UB} / 2$, are supplied as the initial point of the optimization. During the optimization process, objective function and constraint of maximum pressure and maximum tangential stress are assessed by using the kriging surrogate models, which are constructed in previous section. The optimization converges after 42 iterations. The objective function and constraints are evaluated 639 times during the optimization, whereas 304 evaluations are consumed for constructing the kriging model. The optimal values of the design variables are presented in Table 4. The x_2 and x_3 converge to their lower boundary, and the remaining variables converge between their upper and lower boundaries. Shape of the optimal design is provided in Fig. 15. It can be confirmed that thicknesses of outer parts of the RMS are increased to relieve the maximum tangential

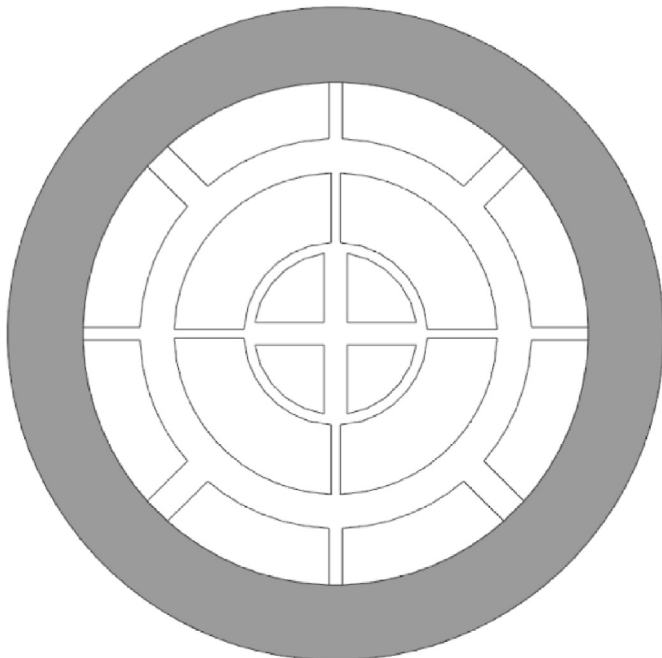


Fig. 15. Shape of the optimal design.

Table 5

Performances of the optimal design.

	Function	Formulation	Optimal design		Unit
			Kriging	Analysis	
Objective function	$P_{\max}(\mathbf{x})$	Minimize	2.96	3.81	kbar
Constraint	$V_{EM}(\mathbf{x})$	$\geq 2.437e6$	2.562e6	–	–
	σ_{case}	≤ 1.095	0.950	1.063	GPa

stress. Table 5 presents the variation in the performances in the formulation. The performances, which are assessed by the kriging models in the optimization, are assessed by the finite element model for verification. The maximum pressure of the energetic material decreases from 3.46 kbar to 2.96 kbar in the optimization. However, with the finite element model, the optimal design yields 3.81 kbar. The difference is caused by the error in the kriging model. As a result, the maximum pressure increases by 10% from that of the smoothed shape of the topology optimization. The volume of the energetic material satisfies the constraint. The maximum tangential stress of the case decreases from 1.236 GPa to 950.4 MPa, and the constraint is satisfied. With the finite element analysis, the maximum stress increases to 1.063 GPa. Nonetheless, it still satisfies the constraint. The difference between the kriging model and the finite element model can be reduced by constructing a more accurate surrogate model or employing finite element analysis in the optimization. However, because higher computational cost is incurred in the reduction, the trade-off between accuracy and computational cost should be considered. As a result, the optimal design of the RMS and steel case is derived using size optimization. Although the maximum pressure is increased, the maximum stress constraint, which is infeasible in the smoothed shape, becomes feasible here.

4. Conclusion

In this study, design optimization of an RMS is performed to maximize the impact resistance of a penetrative projectile, and an optimal design of the RMS and steel case is derived. The high cost penetration test is replaced with finite element analysis, to perform the design optimization. The finite element model is constructed with appropriate material models of each component of the target and projectile. To achieve accuracy of the finite element analysis, a parameter, namely, the maximum principal strain for element erosion, is calibrated by comparing the residual velocity of the projectile with the experimental result. As a result, the finite element model is calibrated with 0.44% error in residual velocity.

Based on the analysis model, the topology optimization is introduced to derive shape of the RMS. The limitations in the manufacture of the RMS are considered to achieve the producible shape of the RMS. The manufacturing constraints are investigated, and the design variables and formulation are proposed considering these constraints. As a result, the optimal shape, which maximizes the impact resistance, is derived while satisfying the intended manufacturing constraints. Moreover, the shape is smoothed for the size optimization. As a result, optimal shape of the RMS, which reduces the maximum pressure 60% compared to the baseline, is obtained.

Based on the smoothed design, the dimensions of the RMS, as well as the steel case, are determined through the size optimization. The kriging surrogate model is introduced to save computational cost, and the kriging models of the projectile performances are constructed. The kriging models are employed to assess objective function and constraint of size optimization. Through the optimization, the optimal design of the RMS and steel case, which maximizes the impact resistance, as well as the volume of the energetic material, is determined. The maximum pressure of the energetic material is decreased by 56% from 8.69 kbar to 3.81 kbar, and the volume of the energetic material is increased by 5%. The structural safety of the steel case is maintained by achieving a 3% reduction in the maximum tangential stress.

On the other hand, as mentioned above, the use of cold spray (which is employed in manufacturing RMSs) exhibits low resolution and accuracy in comparison with other manufacturing methods. Therefore, the product dimensions may be different from the intended optimal design, and the projectile's performance may be altered accordingly. Therefore, these uncertainties in the dimensions of an RMS should be considered in the future. Furthermore, the application of design methods taking into account uncertainties (such as reliability-based design optimization and robust design optimization) should be considered. Additionally, actual performances of the optimum design is not investigated through experiment, because the manufacturing techniques of the RMS immature. Therefore, actual performance of the optimized structures should be investigated in the future.

Declaration of competing interest

The authors declare that they have no known competing financial interests or personal relationships that could have appeared to influence the work reported in this paper.

Acknowledgments

This study was supported by the Agency for Defense Development, Republic of Korea [grant number UD170110GD].

References

- [1] Becuwe A, Delclos A. Low-sensitivity explosive compounds for low vulnerability warheads. *Propellants, Explos Pyrotech* 1993;18:1–10. <https://doi.org/10.1002/prep.19930180102>.
- [2] Roy PK, Ramarao K. Computer code for evaluation of design parameters of concrete piercing earth shock missile warhead. *Defence Sci J* 1985;35:401–9. <https://doi.org/10.14429/dsj.35.6041>.
- [3] Hastings DL, Dreizin EL. Reactive structural materials: preparation and characterization. *Adv Eng Mater* 2018;20:1700631. <https://doi.org/10.1002/adem.201700631>.
- [4] Peiris SM. Enhancing energy in future conventional munitions using reactive materials. *AIP Conf. Proc.*, vol. 1979. American Institute of Physics; 2018, 020002. <https://doi.org/10.1063/1.5044770>.
- [5] Bacciochini A, Bourdon-Lafleur S, Poupard C, Radulescu M, Jodoin B. Ni-Al nanoscale energetic materials: phenomena involved during the manufacturing of bulk samples by cold spray. *J Therm Spray Technol* 2014;23:1142–8. <https://doi.org/10.1007/s11666-014-0078-1>.
- [6] Byun G, Kim J, Lee C, Kim SJ, Lee S. Kinetic spraying deposition of reactive-enhanced Al-Ni composite for shaped charge liner applications. *J Therm Spray Technol* 2016;25:483–93. <https://doi.org/10.1007/s11666-015-0368-2>.
- [7] Bacciochini A, Radulescu MI, Youndouzi M, Maines G, Lee JJ, Jodoin B. Reactive structural materials consolidated by cold spray: Al-CuO thermite. *Surf Coating Technol* 2013;226:60–7. <https://doi.org/10.1016/j.surfcoat.2013.03.036>.
- [8] Dean SW, Potter JK, Yetter RA, Eden TJ, Champagne V, Trexler M. Energetic intermetallic materials formed by cold spray. *Intermetallics* 2013;43:121–30. <https://doi.org/10.1016/j.intermet.2013.07.019>.
- [9] Grujicic M, Saylor JR, Beasley DE, DeRosset WS, Helfritsch D. Computational analysis of the interfacial bonding between feed-powder particles and the substrate in the cold-gas dynamic-spray process. *Appl Surf Sci* 2003;219:211–27. [https://doi.org/10.1016/S0169-4332\(03\)00643-3](https://doi.org/10.1016/S0169-4332(03)00643-3).
- [10] Grujicic M, Zhao CL, DeRosset WS, Helfritsch D. Adiabatic shear instability based mechanism for particles/substrate bonding in the cold-gas dynamic-spray process. *Mater Des* 2004;25:681–8. <https://doi.org/10.1016/j.matdes.2004.03.008>.
- [11] Sova A, Grigoriev S, Okunkova A, Smurov I. Potential of cold gas dynamic spray as additive manufacturing technology. *Int J Adv Manuf Technol* 2013;69:2269–78. <https://doi.org/10.1007/s00170-013-5166-8>.
- [12] Raelison RN, Verdy C, Liao H. Cold gas dynamic spray additive manufacturing today: deposit possibilities, technological solutions and viable applications. *Mater Des* 2017;133:266–87. <https://doi.org/10.1016/j.matdes.2017.07.067>.
- [13] Lynch ME, Gu W, El-Wardany T, Hsu A, Viens D, Nardi A, et al. Design and topology/shape structural optimisation for additively manufactured cold sprayed components. *Virtual Phys Prototyp* 2013;8:213–31. <https://doi.org/10.1080/17452759.2013.837629>.
- [14] Yin S, Cavaliere P, Aldwell B, Jenkins R, Liao H, Li W, et al. Cold spray additive manufacturing and repair: fundamentals and applications. *Addit Manuf* 2018;21:628–50. <https://doi.org/10.1016/j.addma.2018.04.017>.
- [15] Lu D, Wang H, Lei M, Yu Q. Enhanced initiation behavior of reactive material projectiles impacting covered explosives. *Propellants, Explos Pyrotech* 2017;42:1117–23. <https://doi.org/10.1002/prep.201700063>.
- [16] Xu FY, Zheng YF, Yu QB, Zhang XP, Wang HF. Damage effects of aluminum plate by reactive material projectile impact. *Int J Impact Eng* 2017;104:38–44. <https://doi.org/10.1016/j.ijimpeng.2017.02.010>.
- [17] Kotei DA. Aluminum reactive material warhead casings. *Naval Postgraduate School*; 2018.
- [18] Graves WT, Liu D, Palazotto AN. Impact of an additively manufactured projectile. *J Dyn Behav Mater* 2017;3:362–76. <https://doi.org/10.1007/s40870-017-0102-x>.
- [19] Provchy ZA, Palazotto AN, Flater PJ. Topology optimization for projectile design. *J Dyn Behav Mater* 2018;4:129–37. <https://doi.org/10.1007/s40870-018-0143-9>.
- [20] Patel AA, Palazotto AN. Design methodology for topology optimization of dynamically loaded structure. *J Dyn Behav Mater* 2019;5:59–64. <https://doi.org/10.1007/s40870-019-00184-0>.
- [21] Liang K, Huang Z, Zhang J. Optimal design of the aerodynamic parameters for a supersonic two-dimensional guided artillery projectile. *Def Technol* 2017;13:206–11. <https://doi.org/10.1016/j.dt.2017.05.003>.
- [22] Zhao Q, Chen Z, Huang Z, Zhang H, Ma J. Optimization of the aerodynamic configuration of a tubular projectile based on blind Kriging. *Sci Iran* 2019;26:311–22. <https://doi.org/10.24200/sci.2017.20015>.
- [23] Jinseok K. Extended range of a projectile using optimization of body shape. *J Korea Soc Simul* 2020;29:49–55. <https://doi.org/10.9709/JKSS.2020.29.3.049>.
- [24] Murray Y. Users manual for LS-DYNA concrete material model 159. United states: federal highway administration. Office of Research, Development, and Technology; 2007.
- [25] Murray Y, Abu-Odeh A, Bligh R. Evaluation of LS-DYNA concrete material model 159. United states: federal highway administration. Office of Research, Development, and Technology; 2007.
- [26] Holmquist TJ, Johnson GR. A computational constitutive model for glass subjected to large strains, high strain rates and high pressures. *J Appl Mech* 2011;78. <https://doi.org/10.1115/1.4004326>.
- [27] Malvar LJ, Crawford JE, Morrill KB. K&C concrete material model release III-automated generation of material model input (2000TR-99-24-B1). 2000.
- [28] Schwer LE, Malvar LJ. Simplified concrete modeling with* MAT_CONCRETE_DAMAGE_REL3. JRI LS-dyna user week. Bamberg: LS-DYNA Anwenderforum; 2005. p. 49–60.
- [29] Mohammed TA, Parvin A. Evaluating damage scale model of concrete materials using test data. *Adv Concr Constr* 2013;1:289. <https://doi.org/10.12989/acc2013.1.4.289>.
- [30] Johnson GR, Cook WH. Fracture characteristics of three metals subjected to various strains, strain rates, temperatures and pressures. *Eng Fract Mech* 1985;21:31–48.
- [31] He A, Xie G, Zhang H, Wang X. A comparative study on Johnson–Cook, modified Johnson–Cook and Arrhenius-type constitutive models to predict the high temperature flow stress in 20CrMo alloy steel. *Mater Des* 2013;52:677–85. <https://doi.org/10.1016/j.matdes.2013.06.010>.
- [32] Hallquist JO. LS-DYNA® keyword user's manual volume II material models. USA: California; 2013.
- [33] Dietenberger M, Buyuk M, Kan CD. Development of a high strain-rate dependent vehicle model. Bamberg; 2005.
- [34] Grüneisen E. Theorie des festen Zustandes einatomiger Elemente. *Ann Phys* 1912;344:257–306. <https://doi.org/10.1002/andp.19123441202>.

- [35] Lemons DS, Lund CM. Thermodynamics of high temperature, Mie–Grüneisen solids. *Am J Phys* 1999;67:1105–8. <https://doi.org/10.1119/1.19091>.
- [36] Chen TH, Wu JH. Mechanical behavior and fracture properties of NiAl intermetallic alloy with different copper contents. *Appl Sci* 2016;6:70. <https://doi.org/10.3390/app6030070>.
- [37] Khoe YS, Weerheijm J. Limitations of smeared crack models for dynamic analysis of concrete. 12th Int. LS-DYNA Users Conf. Const. Model. 2012.
- [38] Bendsøe MP, Sigmund O. *Topology optimization: theory, methods, and applications*. Springer Science & Business Media; 2013.
- [39] Bendsøe MP, Sigmund O. Material interpolation schemes in topology optimization. *Arch Appl Mech* 1999;69:635–54. <https://doi.org/10.1007/s004190050248>.
- [40] Wang MY, Wang X, Guo D. A level set method for structural topology optimization. *Comput Methods Appl Mech Eng* 2003;192:227–46. [https://doi.org/10.1016/S0045-7825\(02\)00559-5](https://doi.org/10.1016/S0045-7825(02)00559-5).
- [41] Choi WS, Park GJ. Structural optimization using equivalent static loads at all time intervals. *Comput Methods Appl Mech Eng* 2002;191:2105–22. [https://doi.org/10.1016/S0045-7825\(01\)00373-5](https://doi.org/10.1016/S0045-7825(01)00373-5).
- [42] Goldberg DE, Holland JH. Genetic algorithms and machine learning. *Mach Learn* 1988;3:95–9. <https://doi.org/10.1177/0954408914531118>.
- [43] Kawamura H, Ohmori H, Kito N. Truss topology optimization by a modified genetic algorithm. *Struct Multidiscip Optim* 2002;23:467–73. <https://doi.org/10.1007/s00158-002-0208-0>.
- [44] Kennedy J, Eberhart R. Particle swarm optimization. *Proc. ICNN'95-Int Conf Neural Networks* 1995;4:1942–8. IEEE.
- [45] Luh G-C, Lin C-Y, Lin Y-S. A binary particle swarm optimization for continuum structural topology optimization. *Appl Soft Comput* 2011;11:2833–44. <https://doi.org/10.1016/j.asoc.2010.11.013>.
- [46] Karaboga D, Basturk B. In: Melin P, Castillo O, Aguilar LT, Kacprzyk J, Pedrycz W, editors. *Artificial Bee Colony (ABC) Optimization Algorithm for Solving Constrained Optimization Problems BT - Foundations of Fuzzy Logic and Soft Computing*. Berlin, Heidelberg: Springer Berlin Heidelberg; 2007. p. 789–98.
- [47] Fang J, Sun G, Qiu N, Steven GP, Li Q. Topology optimization of multicell tubes under out-of-plane crushing using a modified artificial bee colony algorithm. *J Mech Des* 2017;139. <https://doi.org/10.1115/1.4036561>.
- [48] Karaboga D, Basturk B. A powerful and efficient algorithm for numerical function optimization: artificial bee colony (ABC) algorithm. *J Global Optim* 2007;39:459–71. <https://doi.org/10.1007/s10898-007-9149-x>.
- [49] Sacks J, Welch WJ, Mitchell TJ, Wynn HP. Design and analysis of computer experiments. *Stat Sci* 1989;4:409–23.
- [50] Park J-S. Optimal Latin-hypercube designs for computer experiments. *J Stat Plann Inference* 1994;39:95–111. [https://doi.org/10.1016/0378-3758\(94\)90115-5](https://doi.org/10.1016/0378-3758(94)90115-5).
- [51] Johnson ME, Moore LM, Ylvisaker D. Minimax and maximin distance designs. *J Stat Plann Inference* 1990;26:131–48. [https://doi.org/10.1016/0378-3758\(90\)90122-B](https://doi.org/10.1016/0378-3758(90)90122-B).
- [52] Meckesheimer M, Booker AJ, Barton RR, Simpson TW. Computationally inexpensive metamodel assessment strategies. *AIAA J* 2002;40:2053–60. <https://doi.org/10.2514/2.1538>.
- [53] Boggs PT, Tolle JW. Sequential quadratic programming. *Acta Numer* 1995;4:1–51. <https://doi.org/10.1017/S0962492900002518>.